Nanoscale

PAPER

Cite this: *Nanoscale*, 2026, **18**, 9846

Enhanced peroxidase-like activity of palladium–iron bimetallic nanoparticles supported on N-doped mesoporous carbon for colorimetric detection of ascorbic acid and dopamine

Zahra Bahreini,[a] Siyavash Kazemi Movahed, *[a] Keun Hwa Chae *[b] and Cheol-Hwee Shim [b]

Received 4th January 2026,
Accepted 20th March 2026

DOI: 10.1039/d6nr00031b

rsc.li/nanoscale

Nanozymes, despite their promising stability and cost-effectiveness, often suffer from lower catalytic activity compared to natural enzymes, limiting their practical applications. Herein, we report the rational design, synthesis, and comprehensive characterization of novel bimetallic palladium–iron nanoparticles supported on nitrogen-doped mesoporous carbon (Fe–Pd@N-MC) as a highly efficient peroxidase-mimicking nanozyme. Structural and morphological analyses using XRD, HR-TEM, XPS, and N_2 physisorption confirmed the successful formation of uniformly dispersed, superparamagnetic bimetallic nanoparticles composed of Pd^0 and Fe_3O_4. Benefiting from the synergistic effect between Pd and Fe species, Fe–Pd@N-MC exhibited markedly enhanced peroxidase-like activity compared to its monometallic counterparts (Fe@N-MC and Pd@N-MC) toward both 3,3′,5,5′-tetramethylbenzidine (TMB) and *o*-phenylenediamine (OPD). Kinetic studies revealed excellent catalytic efficiency and high substrate affinity, with K_m values of 0.156 mM for TMB and 0.088 mM for OPD. Mechanistic investigations identified hydroxyl radicals (˙OH) as the dominant reactive species driving the oxidation processes. Exploiting its robust and rapid catalytic performance, Fe–Pd@N-MC was further employed to construct a sensitive and selective colorimetric platform for the detection of dopamine and ascorbic acid, achieving limits of detection of 3.44 μM and 2.87 μM, respectively. The practical applicability of this nanozyme-based sensor was demonstrated through the accurate quantification of ascorbic acid in fresh fruit juice samples, highlighting its potential for application in biosensing, food analysis and clinical diagnostics.

Introduction

Natural enzymes are remarkable biocatalysts that catalyze a wide range of biological processes with high selectivity and efficiency. Their highly selective and efficient catalytic activity has made them essential in diverse applications, such as biosensors, the food industry, medical diagnostics, and biofuel production.[1,2] However, their use is limited by several inherent challenges, including poor operational stability, high production costs, storage difficulties, and complex purification requirements.[3–5] To address these limitations, researchers have extensively studied nanomaterials that mimic enzymatic function. These artificial alternatives, known as nanozymes, overcome many of the limitations of their biological counterparts while maintaining comparable catalytic functions.

Nanozymes can be classified based on their enzyme-like activities, which resemble those of natural enzymes such as superoxide dismutase, peroxidase, oxidase, and catalase.[6,7] Among these enzyme-mimetic activities, peroxidase-like activity has shown considerable promise in applications ranging from pollutant detection and degradation to bioremediation, biosensors, disease diagnosis and treatment, and industrial catalysis.[8–12] Redox-active nanozymes have been intensively investigated for their ability to regulate reactive oxygen species (ROS), including superoxide (O_2^-), hydrogen peroxide (H_2O_2), hydroxyl radical (˙OH), and peroxide (O_2^{2-}), in both catalytic and biological redox reactions. Due to their intrinsic peroxidase-like activity, iron-based nanozymes have been widely used to mimic the catalytic function of horseradish peroxidase (HRP).[13] Similarly, palladium nanoparticles have demonstrated significant peroxidase-mimicking

[a]*Department of Chemistry, Isfahan University of Technology, Isfahan 8415683111, Islamic Republic of Iran. E-mail: skazemi@iut.ac.ir; Tel: +98 31 3391 3282*
[b]*Advanced Analysis Center, Korea Institute of Science and Technology (KIST), Seoul 02792, Republic of Korea. E-mail: khchae@kist.re.kr*

properties and have been used in sensitive colorimetric detection assays.[14,15]

Within the expanding repertoire of nanozyme materials, bimetallic nanoparticles have emerged as exceptionally effective catalysts.[16] Their superior performance arises from unique structural and electronic properties, which result from the synergistic interactions between their constituent metals. This synergy enhances their electronic properties and optimizes the binding energies of catalytic intermediates, thereby improving catalytic efficiency.[17] Palladium, a noble metal, is known for its excellent catalytic properties, particularly in oxidation reactions such as methane oxidation, hydrocarbon oxidation, CO oxidation, and alcohol oxidation.[18–22] The combination of palladium with iron oxides enhances catalytic performance through several mechanisms, including strong metal–support interactions,[23] improved dispersion,[24] bimetallic synergy,[25] morphological effects,[26] and increased stability and reusability.[27] Palladium/iron oxide systems demonstrate superior performance in peroxidase-like reactions and other catalytic processes due to several factors, including enhanced electron transfer between Pd and Fe species,[23,28] generation of active sites at the metal–metal oxide interface,[26,29] promotion of ROS formation (crucial for peroxidase activity),[30,31] and facilitated magnetic separation, which enables catalyst reuse.[32,33]

The catalytic performance of bimetallic nanoparticles can be further enhanced by carefully selecting support materials. Nitrogen-doped mesoporous carbon serves as an excellent support material, offering several advantages for catalytic applications. Its high surface area provides an abundance of active sites for catalytic reactions, while the presence of nitrogen functionalities introduces additional active sites within the carbon framework. These nitrogen functional groups interact with the metal nanoparticles to improve their dispersion, stability, and catalytic performance through multiple mechanisms, such as facilitating electron transfer between the support and the metal nanoparticles, creating defect sites that act as anchors to prevent particle aggregation, and maintaining high dispersion of the catalytic species. The mesoporous structure ensures the efficient mass transport of reactants and products, while the material's high electrical conductivity also facilitates electron transfer processes that are critical for peroxidase-like activity. Palladium–iron bimetallic nanoparticles supported on nitrogen-doped carbon exhibit enhanced catalytic activity due to their increased surface area, improved dispersion of active sites, and more efficient electron transfer.[34–37]

Based on the above introduction and as part of our ongoing studies on carbon-based catalysts, the present study reports the synthesis and characterization of novel Pd–Fe bimetallic nanoparticles supported on nitrogen-doped mesoporous carbon (N-MC), as well as their evaluation for peroxidase-like activity. These hybrid systems could offer increased catalytic efficiency due to interactions between the metals and the support. The materials were thoroughly characterized, and their peroxidase-like activity was evaluated using chromogenic substrates, such as 3,3′,5,5′-tetramethylbenzidine (TMB) and *o*-phenylenediamine (OPD).

Results and discussion

X-ray diffraction (XRD) analysis was performed to study the phases and crystallinity of the synthesized structures (Fig. 1a). The N-MC structure exhibited a broad diffraction peak at 2θ = 26°, which corresponds to the (002) carbon diffraction plane. The absence of discernible diffraction peaks related to iron and iron species in the XRD pattern of the Fe@N-MC structure is probably due to the small size of the nanoparticles and their low content in the catalyst. The XRD pattern of the Pd@N-MC structure showed three main peaks at 2θ = 40°, 47°, and 68°. These peaks were indexed to the (111), (200), and (220) crystal planes of palladium (JCPDS reference code: 01-087-0643). The bimetallic FePd@N-MC structure showed the characteristic palladium peaks, as well as three additional small diffraction peaks at 2θ = 36°, 57°, and 63°, which correspond to the (311), (511), and (440) crystal planes of Fe_3O_4 (JCPDS reference code: 00-002-1035). The presence of magnetite peaks in the bimetallic structure suggested an increase in nanoparticle size.

The pore characteristics of the synthesized structures were evaluated using nitrogen physisorption analysis (Fig. 1b). The N_2 isotherm of the N-MC structure exhibited two distinctive features. First, it showed a steep uptake at relative pressures $p/p_0 < 0.1$, which indicates the presence of microporosity. Second, it exhibited an H2(a)-type hysteresis loop behavior, which is characteristic of ordered mesoporous structures.[38] Additionally, the adsorption and desorption branches did not close, which is a phenomenon commonly observed in some porous carbon materials.[39] Additionally, the sharp increase in N_2 adsorption at high relative pressure ($p/p_0 > 0.95$) indicated multilayer adsorption on the outer surfaces of the support.[40] After metal incorporation, the surface area decreased from 390.7 $m^2\ g^{-1}$ for N-MC to 7.5 $m^2\ g^{-1}$ for Fe@N-MC, 14.9 $m^2\ g^{-1}$ for Pd@N-MC, and 15.4 $m^2\ g^{-1}$ for FePd@N-MC, respectively. This reduction in surface area corresponded to partial pore filling and blockage by metal nanoparticles, thereby reducing pore accessibility. The absence of strong nitrogen uptake at low relative pressure ($p/p_0 < 0.1$) after metal immobilization indicates a significant reduction in microporosity. This suggests that the metal nanoparticles have preferentially deposited in or blocked access to the micropores (pores < 2 nm). These results are probably due to more substantial confinement effects; metal precursors tend to occupy the smallest pores first.[41,42] From a catalytic perspective, pore confinement has dual consequences. First, it restricts the diffusion of reactant molecules toward the active metal sites, which can result in mass transfer limitations and affect the overall reaction rate. Second, confining FePd nanoparticles within a mesoporous carbon framework creates a localized microenvironment around active sites, thereby enriching the substrate. This increases the concentration of local reactants and intermediates, stabilizes the nanoparticles against aggregation, and pro-

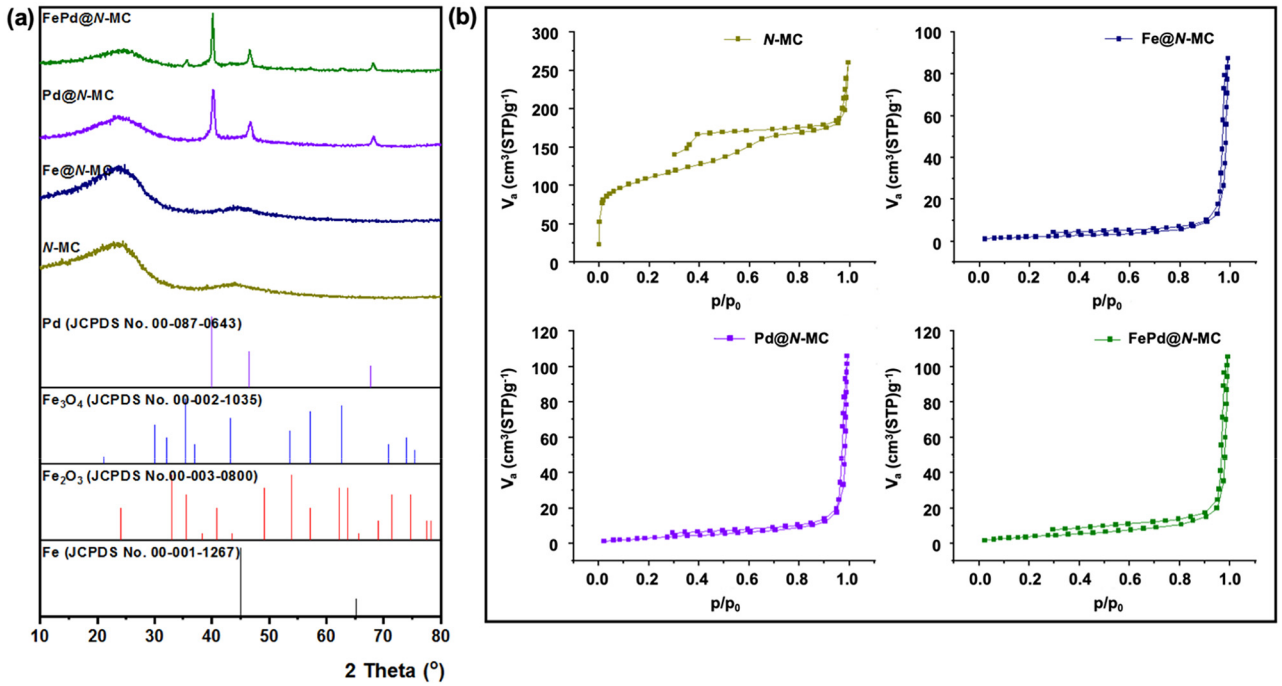

Fig. 1 (a) XRD patterns and (b) nitrogen physisorption analysis of N-MC, Fe@N-MC, Pd@N-MC, and FePd@N-MC.

motes electronic interactions between the metal and the nitrogen-doped carbon support. Thus, despite the significant reduction in surface area, the geometric confinement of nanoparticles within the porous structure is expected to play a critical role in modulating the accessibility of active sites and the rate of mass transfer, and ultimately, the catalytic kinetics.[43–45]

X-ray photoelectron spectroscopy (XPS) was used to analyze the surface composition of the synthesized samples and determine their chemical and electronic states. The XPS survey spectra of the synthesized materials showed the characteristic C 1s, N 1s and O 1s core levels for the N-doped mesoporous carbon support (Fig. 2a). The high-resolution spectrum of the N 1s core level of the synthesized materials was deconvoluted into four peaks at 398.3 eV, 399.8 eV, 400.7 eV, and 402.8 eV, which correspond to *N*-pyridinic, *N*-pyrrolic, *N*-graphitic, and *N*-oxide species, respectively (Fig. 2b).[46] The Fe 2p core level exhibited two multiplet sets corresponding to the two electronic states of Fe^{2+} and Fe^{3+}, which are attributed to the two different oxidation states of iron in the Fe_3O_4 structure (Fig. 2c).[47] The Pd $3d_{5/2}$ core level of the Pd-based synthesized materials showed two different oxidation states of Pd (Fig. 2d). The peaks at 335.2 eV (93%) and 338.0 eV (7%), which are

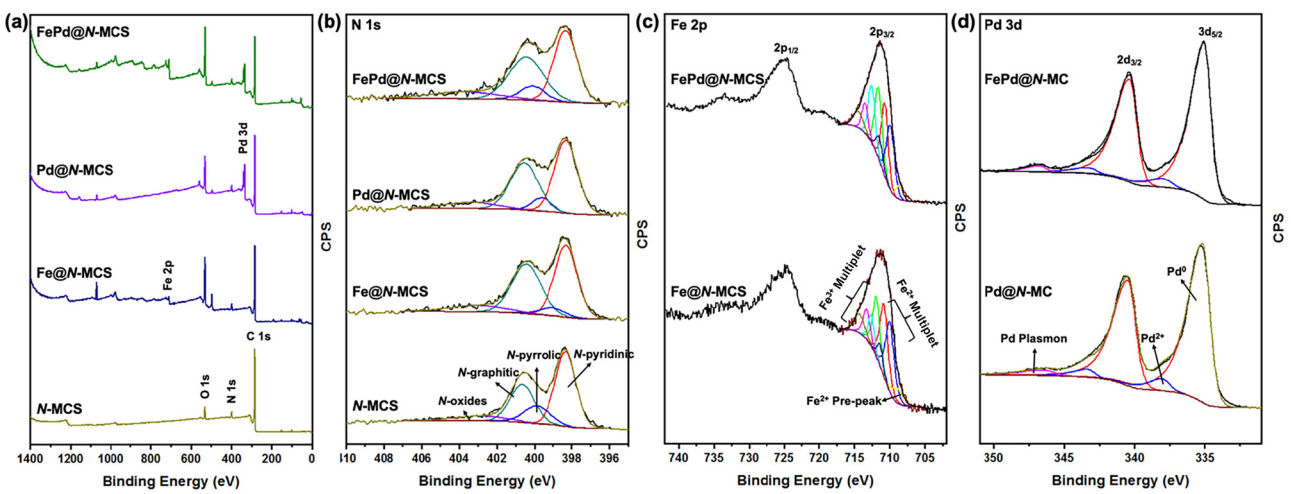

Fig. 2 XPS (a) survey, (b) N 1s core level, (c) Fe 2p core level, and (d) Pd 3d core level spectra of N-MC, Fe@N-MC, Pd@N-MC, and FePd@N-MC.

attributed to Pd^0 and Pd^{2+}, respectively, indicate that the reduction of palladium was successful. The presence of Pd^{2+} species is probably due to surface oxidation of the Pd nanoparticles. The peak at 346.4 eV is most likely a plasmon loss band related to the peak at 335.2 eV, and the plasmon energy of 11.2 eV may be due to the small particle size.[48]

The magnetic properties of the synthesized materials were evaluated using a vibrating sample magnetometer (VSM) (Fig. S1). The Fe@N-MC sample showed distinct superparamagnetic behavior, with a saturation magnetization of 1.04 emu g^{-1}, characterized by the absence of a hysteresis loop and a coercivity value close to zero.[49] This behavior arises from the small size of the Fe_3O_4 nanoparticles, where each particle essentially behaves as a single magnetic domain.[50,51] The observed magnetization is significantly lower than that of bulk Fe_3O_4 (92 emu g^{-1}), probably due to nanoparticle confinement within the mesochannels, small particle size, and the relatively low iron content of the composite structure.[52–54] The Pd@N-MC sample exhibited very weak paramagnetic behavior, consistent with the expected magnetic properties of palladium-based materials. The bimetallic FePd@N-MC sample displayed superparamagnetic behavior but with a slightly lower saturation magnetization (0.95 emu g^{-1}). The saturation magnetization of the bimetallic sample was expected to be approximately half that of the monometallic sample, corresponding to half the weight percentage of iron in the bimetallic sample compared to the monometallic iron sample. However, this value is higher than expected, which probably corresponds to synergistic electronic interactions between the two metals and electronic structure modification.[55]

The surface morphology of the synthesized structures was studied using field emission scanning electron microscopy (FE-SEM) (Fig. 3 and Fig. S2). The 3-aminophenol–formaldehyde polymer (AFP) precursors showed a spherical morphology with dimensions of approximately 500 nm (Fig. S2). After the pyrolysis process, the dimensions of the structures decreased to 350 nm due to the loss of volatile components and the carbonization process (Fig. 3a). The introduction of metal species did not significantly alter the surface morphology of the structures. Energy-dispersive X-ray spectroscopy (EDS) was utilized to analyze the elemental distribution of the structures shown in the FE-SEM images. EDS analysis confirmed the presence of nitrogen as a dopant in the carbon structure of all samples, as well as the successful dispersion of iron and palladium in both monometallic and bimetallic structures (Fig. S3–S5). Transmission electron microscopy (TEM) was used to study the structural features and the size distribution of the metal species. The TEM images revealed

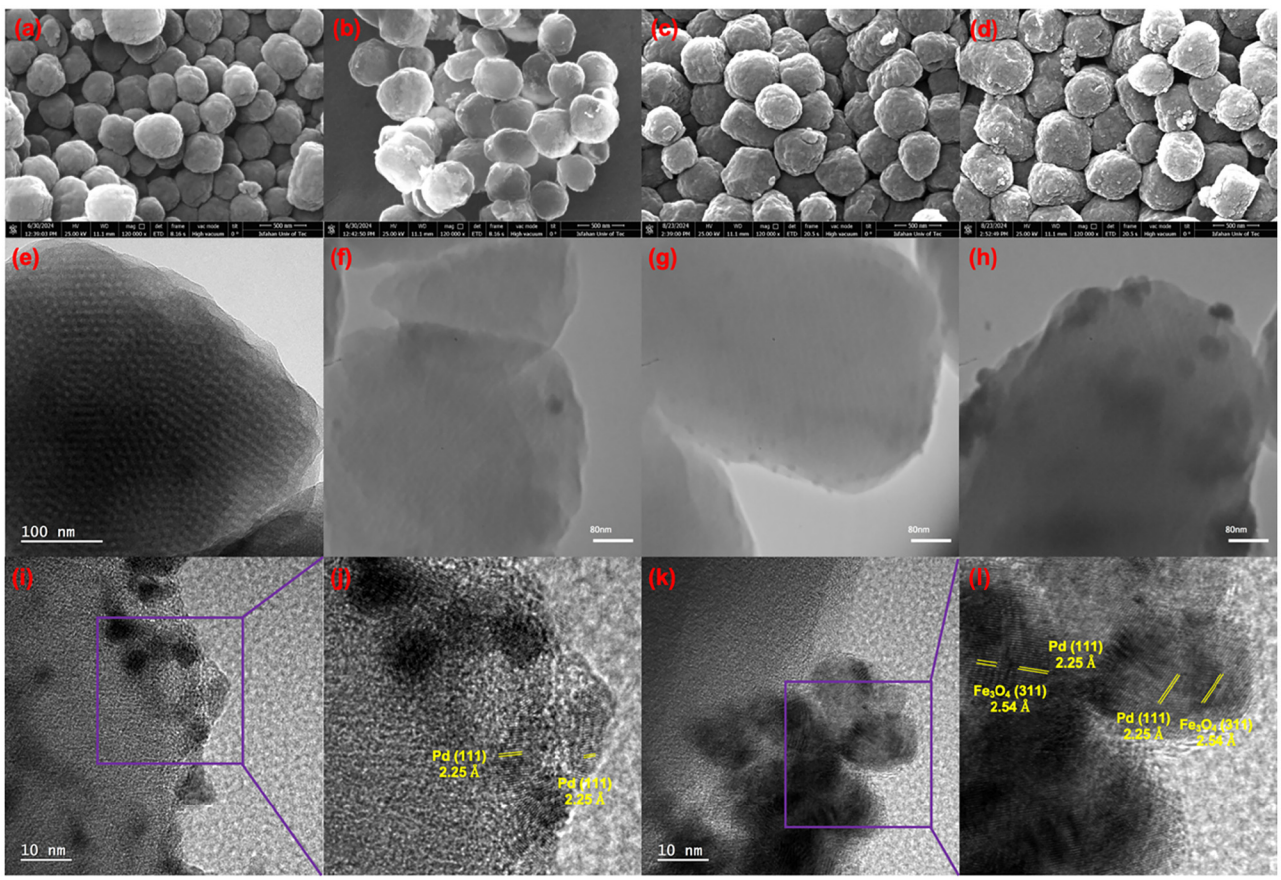

Fig. 3 FESEM images of (a) N-MC, (b) Fe@N-MC, (c) Pd@N-MC, and (d) FePd@N-MC; TEM images of (e) N-MC, (f) Fe@N-MC, (g) Pd@N-MC, and (h) FePd@N-MC; HRTEM images of (i and j) Pd@N-MC and (k and l) FePd@N-MC.

distinct mesoporous channels within the nanostructures (Fig. 3 and Fig. S6). These mesoporous channels enhance catalytic performance by providing an increased surface area, improved mass transfer of reactants and products, and facilitated accessibility to active sites.[56,57] Metal nanoparticles were clearly visible as dark spots in the TEM images. Fe_3O_4 showed larger nanoparticles (30–40 nm) compared to Pd nanoparticles (9–10 nm). In the bimetallic system, the size of the nanoparticles (45–55 nm) was larger than that in the monometallic systems. This increase in nanoparticle size was consistent with the XRD results. The larger particle size of the bimetallic structure compared to its monometallic counterparts can be attributed to the altered nucleation and growth kinetics during synthesis, resulting from the introduction of a second metal species. The high-resolution TEM (HR-TEM) images of Pd@N-MC demonstrated a lattice spacing of 2.25 Å for the Pd nanoparticles, corresponding to the (111) plane (Fig. 3i and j). The HR-TEM image of the FePd@N-MC structure showed lattice spacing of 2.54 Å and 2.25 Å for the Fe_3O_4 and Pd nanoparticles, respectively. These spacings correspond to the (311) crystalline plane of Fe_3O_4 and the (111) crystalline plane of Pd, respectively (Fig. 3k and l).

The peroxidase-like activity of FePd@N-MC was investigated in the oxidation of TMB over a pH range of 3 to 7 using a citrate buffer solution (Fig. 4a). The formation of the charge-transfer diamine–diimine complex (ox-TMB) was monitored by measuring the absorbance at the characteristic wavelength (λ_{max}: 652 nm) after 10 minutes. The appearance of a blue

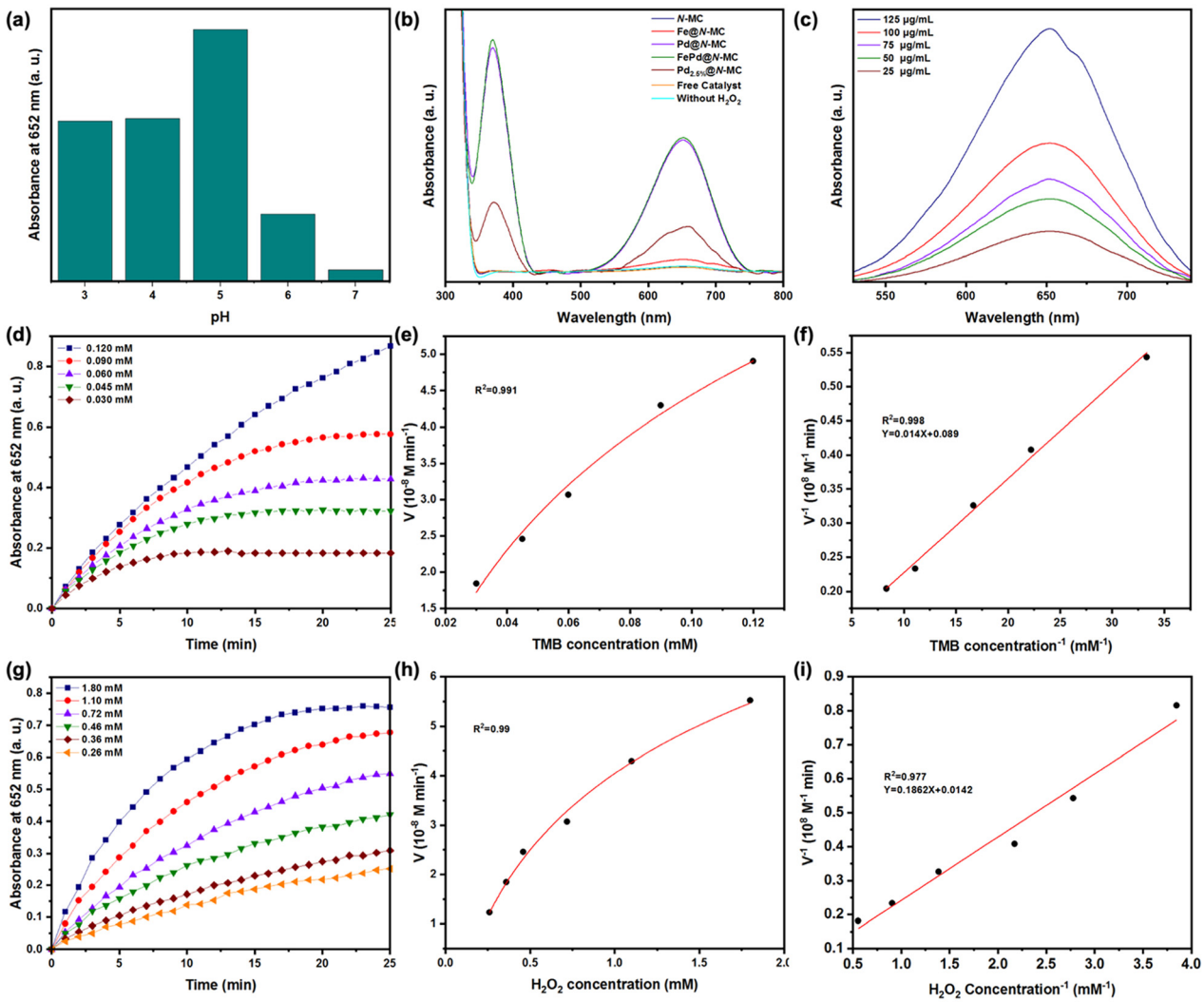

Fig. 4 (a) pH optimization, (b) study of the catalytic activity of the synthesized structures in the peroxidation of TMB and control experiments, (c) peroxidase activity of different amounts of the FePd@N-MC nanozyme suspension, and steady-state kinetic analysis of the peroxidase-like activity of the FePd@N-MC nanozyme. (d–f) Substrate dependence studies with varying TMB concentrations (0.030–0.120 mM): (d) Time-dependent absorbance profiles, (e) Michaelis–Menten plot, and (f) Lineweaver–Burk (double reciprocal) plot at a fixed concentration of H_2O_2 (1.10 mM) and FePd@N-MC (100 μg mL^{-1}). (g–i) Oxidant dependence studies with varying H_2O_2 concentrations (0.26–1.80 mM): (g) time-dependent absorbance profiles, (h) Michaelis–Menten plot, and (i) Lineweaver–Burk (double reciprocal) plot at a fixed concentration of TMB (0.09 mM) and FePd@N-MC (100 μg mL^{-1}).

color in the solution indicated nanozyme activity, with maximum absorbance and catalytic activity observed at pH 5, which was subsequently selected as the optimum pH.

Despite the historical significance of iron oxide (Fe_3O_4) as the first reported nanozyme,[58] the monometallic iron-containing structure (Fe@N-MC) exhibited unexpectedly low activity, as evidenced by the low conversion of TMB to ox-TMB and low absorbance at 652 nm (Fig. 4b). This low activity is probably due to the low iron loading. In contrast, the palladium-based nanozyme (Pd@N-MC) showed superior performance with significantly higher absorbance, indicating high catalytic activity. The bimetallic iron–palladium structure (FePd@N-MC) slightly outperformed the monometallic palladium-based nanozyme (Pd@N-MC). While the Fe@N-MC structure showed low peroxidase-like activity, the incorporation of iron into the bimetallic system allowed for comparable or higher activity at a lower palladium content (2.5 wt% Pd in Pd@N-MC *vs.* 5 wt% Pd in Pd@N-MC). To elucidate the synergistic role of iron, a monometallic $Pd_{2.5\%}$@N-MC nanozyme with 2.5 wt% palladium was synthesized, which exhibited significantly lower activity than its bimetallic counterpart with equivalent palladium content. This observation supports the synergistic effect between palladium and iron and confirms the economic advantage of combining noble metals with first-row transition metals. Based on these results, the bimetallic structure was selected for further investigation.

Three control experiments were carried out to examine the role of each reaction component (Fig. 4b). In the absence of hydrogen peroxide, no peak was detected at 652 nm, confirming that H_2O_2 is essential for TMB oxidation and demonstrating that the structure lacks oxidase activity under aerobic conditions. The nanozyme-free and metal-free support showed no evidence of the formation of ox-TMB, which confirmed both the necessity of the catalytic nanozyme and the critical role of the metallic species in the structure.

The relationship between nanozyme concentration and peroxidase activity was investigated (Fig. 4c). A direct correlation was observed, where a reduction in the nanozyme amount was accompanied by a proportional decrease in peak intensity at 652 nm. This decrease in peak intensity with decreasing nanozyme amount is explained by a corresponding reduction in the number of active sites, resulting in a slower reaction rate. This behavior is consistent with enzyme kinetics, where the reaction rate depends on the concentration of active sites. The suspension concentration of 100 μg mL^{-1} was selected as the optimal catalyst concentration for subsequent experiments, providing an ideal balance between catalytic efficiency and efficient nanozyme usage. This concentration showed robust activity while ensuring cost-effective catalyst utilization.

The kinetic behavior of the nanozyme in TMB oxidation in the presence of hydrogen peroxide was systematically investigated at 652 nm. Two sets of experiments were performed to study the effect of TMB and H_2O_2 concentrations on steady-state kinetic parameters (Fig. 4d and g). Based on Michaelis–Menten and Lineweaver–Burk plots, the K_m and V_{max} constants for TMB were calculated to be 0.156 mM and 0.113 μM min^{-1}, respectively (Fig. 4f). Additionally, for H_2O_2, the K_m and V_{max} constants were determined to be 3.323 mM and 0.178 μM min^{-1}, respectively (Fig. 4i). The lower K_m value for TMB compared to that of H_2O_2 suggests stronger affinity of the nanozyme for TMB, indicating more efficient catalysis of the peroxidation reaction.

The peroxidase activity of the nanozyme was also investigated using OPD as a substrate in the presence of hydrogen peroxide. First, to determine the optimal pH, citrate buffer solutions with different pH were used, and the change in absorbance at 450 nm was measured (Fig. 5a). This wavelength corresponds to the λ_{max} of 2,3-diaminophenazine (the oxidative condensation product formed by peroxidase from two OPD molecules), which was monitored after 10 minutes. The color change of the solution to yellow indicated the activity of the synthesized nanozyme and the oxidation of OPD, leading to the formation of 2,3-diaminophenazine. The results revealed that the highest absorbance, and consequently the highest conversion of the substrate and peroxidase activity, occurred at pH 5. Therefore, pH 5 was selected as the optimal pH.

The peroxidase activity of the synthesized catalysts was evaluated, and it was found that the iron-based nanozyme (Fe@N-MC) did not exhibit a characteristic peak for peroxidase activity at 450 nm, which is similar to TMB peroxidation (Fig. 5b). In contrast, the palladium-based nanozyme (Pd@N-MC) displayed a significant absorbance peak, which indicated that palladium possesses nanozyme activity and can catalyze the peroxidation process more effectively than the iron-based nanozyme. The bimetallic nanozyme (FePd@N-MC) showed the highest absorbance, which can be attributed to the synergistic effect of the two metals in this nanozyme. In this combination, the two metals act cooperatively and complementarily to enhance the efficiency of the peroxidation reaction. The $Pd_{2.5\%}$@N-MC nanozyme exhibited lower peroxidase activity than its bimetallic counterpart containing the same weight percentage of palladium.

Control tests were conducted to examine the role of each component of the peroxidation reaction (Fig. 5b). No absorbance peak was observed at 450 nm in the test without hydrogen peroxide, which indicated that it is essential for peroxidation. Additionally, no absorbance peak was observed in the test performed without the nanozyme and with a metal-free support, demonstrating that the nanozyme and metal species are necessary for the peroxidation reaction to occur.

The effect of nanozyme concentration on peroxidase activity and the intensity of the absorbance peak in the UV-Vis spectrum was investigated using suspensions of different concentrations (Fig. 5c). Similar to the TMB peroxidation, the results showed that decreasing nanozyme concentration caused a decrease in nanozyme activity. Therefore, a concentration of nanozyme of 100 μg mL^{-1} was selected for subsequent experiments.

Two sets of experiments were conducted to study the effect of OPD and H_2O_2 concentrations on steady-state kinetic parameters (Fig. 5d and g). The K_m and V_{max} constants for OPD

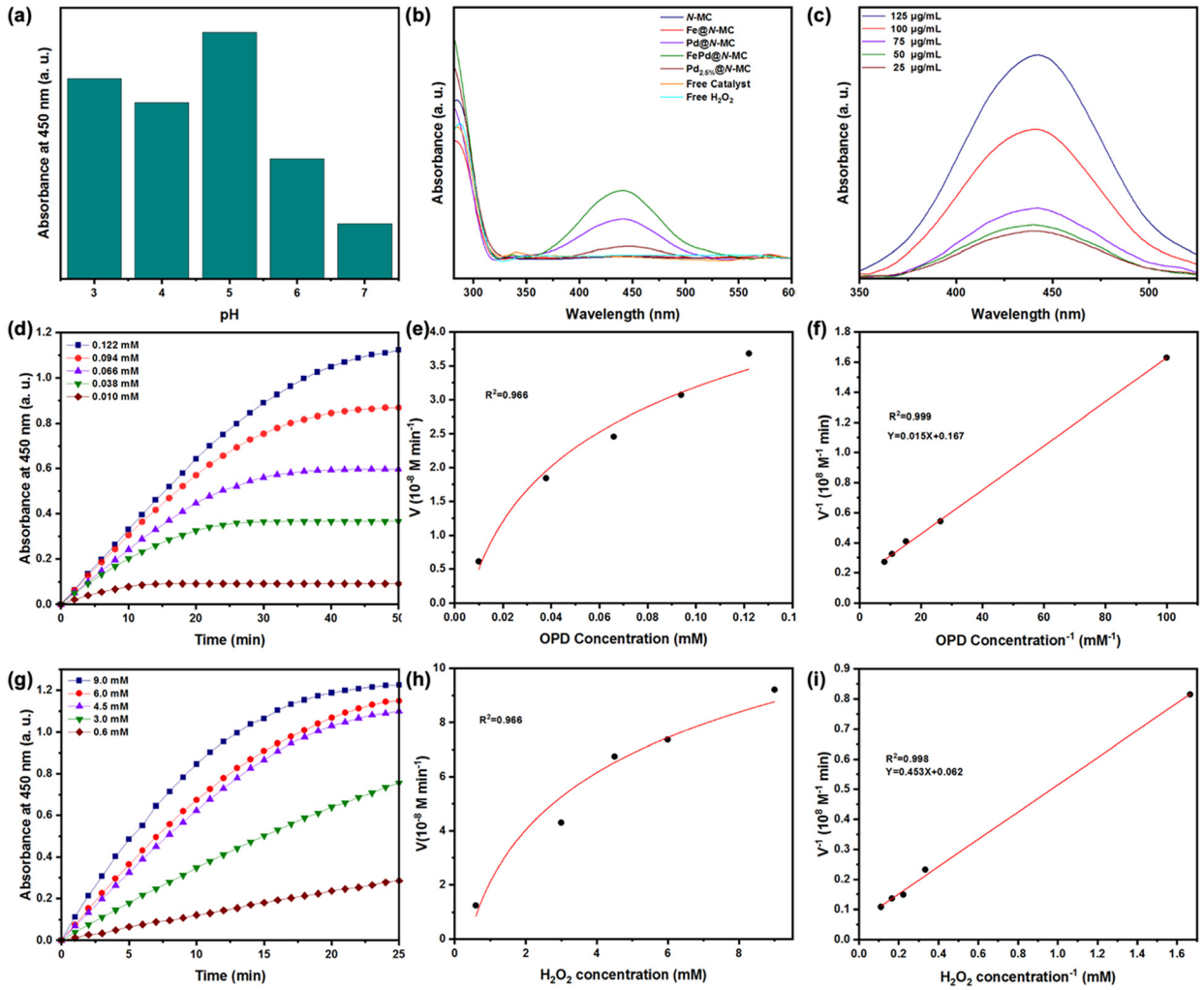

Fig. 5 (a) pH optimization, (b) study of the catalytic activity of the synthesized structures in the peroxidation of OPD and control experiments, (c) peroxidase activity of different amounts of the FePd@N-MC nanozyme suspension, and steady-state kinetic analysis of the peroxidase-like activity of the FePd@N-MC nanozyme. (d–f) Substrate dependence studies with varying OPD concentrations (0.010–0.122 mM): (d) time-dependent absorbance profiles, (e) Michaelis–Menten plot, and (f) Lineweaver–Burk (double reciprocal) plot at a fixed concentration of H_2O_2 (9.0 mM) and FePd@N-MC (100 μg mL^{-1}). (g–i) Oxidant dependence studies with varying H_2O_2 concentrations (0.6–9.0 mM): (g) time-dependent absorbance profiles, (h) Michaelis–Menten plot, and (i) Lineweaver–Burk (double reciprocal) plot at a fixed concentration of OPD (0.122 mM) and FePd@N-MC (100 μg mL^{-1}).

were calculated to be 0.088 mM and 0.163 μM min^{-1}, respectively (Fig. 5f). Additionally, for H_2O_2, the K_m and V_{max} constants were determined to be 7.370 mM and 0.163 μM min^{-1}, respectively (Fig. 5i). The lower K_m value for OPD than for H_2O_2 suggests that the nanozyme has stronger affinity for OPD and can therefore catalyze the peroxidation reaction more efficiently.

Experiments were conducted over four consecutive cycles to evaluate the reusability of the synthesized nanozyme. The catalyst was isolated from the reaction mixture by employing an external magnetic field. Then it was washed with an ethanol–water mixture, followed by drying at ambient temperature. The results showed that while the nanozyme is reusable, its activity did not decrease significantly with each run (Fig. S8). The morphology of the reused nanozyme showed no obvious changes after four consecutive runs, although some agglomeration of nanoparticles was observed (Fig. S9a). Additionally, the XRD pattern of the reused structures showed the characteristic diffraction peaks for palladium (2θ = 40° and 68°) and Fe_3O_4 (2θ = 36°) nanoparticles (Fig. S9b).

To investigate the mechanism of this novel nanozyme, various radical scavengers were used, including thiourea (TU), *p*-benzoquinone (*p*-BQ), and sodium azide (NaN_3) as scavengers for $^{\bullet}OH$, $O_2^{\bullet-}$ and $^1O_2$, respectively (Fig. 6a).[59] The results demonstrated that TU severely inhibited peroxidase activity even at the lowest scavenger concentration. In contrast, NaN_3 showed moderate inhibition, while the addition of *p*-BQ had only a minimal effect at the same concentration. Therefore, $^{\bullet}OH$ is the primary reactive intermediate generated during the catalytic process, which is consistent with the established

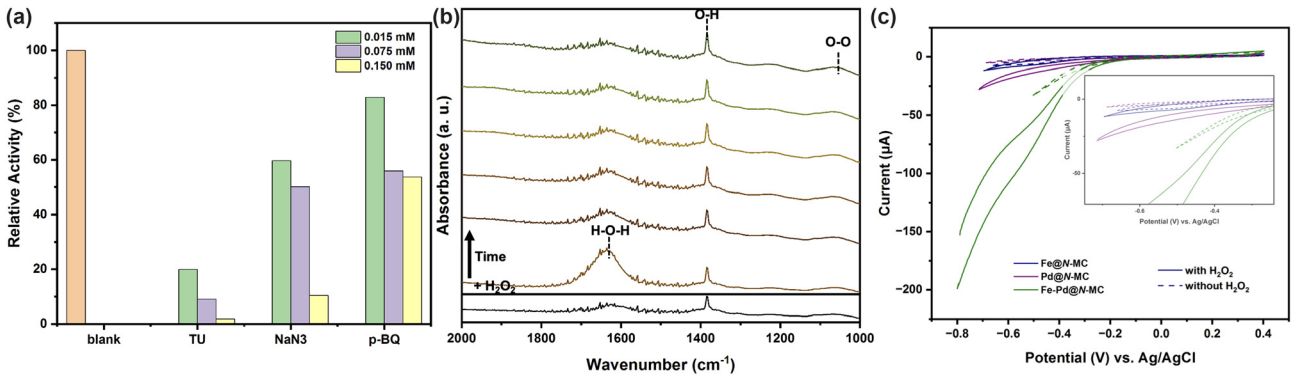

Fig. 6 (a) Control experiments using a series of scavengers, (b) *in situ* FTIR spectra of the catalytic reaction of hydrogen peroxide on FePd@N-MC at different points of time, and (c) CV curves of Fe@N-MC, Pd@N-MC, and FePd@N-MC with (full lines) and without (dotted lines) H_2O_2.

peroxidase mechanism.[59,60] The minimal inhibition by the $O_2^{\bullet-}$ scavenger suggests that it is not a primary species. The moderate inhibition by the $^1O_2$ scavenger suggests that singlet oxygen may also be involved in the reaction mechanism.

The FT-IR spectrum of pristine FePd@N-MC initially showed a signal at 1382 cm^{-1}, corresponding to the phenolic hydroxyl group of the 3-aminophenol precursor (Fig. 6b). Following the addition of hydrogen peroxide, a distinct peak appeared at 1634 cm^{-1}, attributed to the H–O–H bending mode of water. Subsequently, the intensity at 1382 cm^{-1} increased; this change is associated with the O–H bending vibration of surface-adsorbed species, indicating homolytic cleavage of H_2O_2. The growing peak at 1058 cm^{-1}, assigned to the O–O stretching vibration of H_2O_2, confirms the continuous adsorption of H_2O_2 onto the catalyst surface.[61,62] Collectively, these spectroscopic observations confirm that FePd@N-MC exhibits catalytic activity by effectively adsorbing and activating H_2O_2 through a surface-mediated radical generation pathway.

Electrochemical measurements were conducted to evaluate the catalytic activity toward H_2O_2 reduction. As illustrated in Fig. 6c, FePd@N-MC showed a significantly higher reduction current than the monometallic Fe@N-MC and Pd@N-MC samples. This indicates that FePd@N-MC shows excellent H_2O_2 reduction activity.[61,63] FePd@N-MC displayed a sharp cathodic peak, reaching a current response of approximately −200 μA. This magnitude is nearly eighteen and seven times higher than that observed for the monometallic Fe@N-MC and Pd@N-MC, respectively. These results demonstrate a strong synergistic effect between the iron and palladium species in the bimetallic catalyst.

Table 1 shows the kinetic parameters of FePd@N-MC, HRP, and other similar nanozymes, which were examined to compare their affinity for TMB and H_2O_2. The results showed that FePd@N-MC had the lowest K_m for TMB and the highest V_{max}, which could be attributed to the synergistic effect of the simultaneous presence of iron and palladium in these mesoporous structures. Palladium accelerates electron transfer[64,65] and iron improves redox reactions.[66] Additionally, nitrogen doping enhances the catalyst interaction with the substrate, because nitrogen acts as a hydrogen bond acceptor and creates stronger interactions with the substrate.[67,68] These combined effects result in lower K_m and higher V_{max} for FePd@N-MC due to its optimized structure, ultimately leading to improved catalytic efficiency.

Table 1 Comparison of the efficiency of various palladium- and iron-based nanozymes

Nanozyme	Substrate	K_m (mM)	V_{max} ($\times 10^{-8}$ M min^{-1})	Ref.
FePd@N-MC	TMB	0.156	11.27	This study
	H_2O_2	3.23	17.8	
ITO-SiO_2-prS-PdNPs	TMB	0.47	6.10	69
	H_2O_2	0.68	3.79	
Pd nanoclusters	TMB	0.063	0.046	70
	H_2O_2	80.8	0.056	
Pd NPs/CeO_2 NTs	TMB	0.39	5.94	71
	H_2O_2	9.43	1.91	
Pd NPs	TMB	0.74	4.42	71
	H_2O_2	4.50	0.84	
Pd-carbon dots	TMB	0.74	4.6	72
	H_2O_2	10.12	0.72	
N,Fe-carbon dots	TMB	0.40	1.19	73
	H_2O_2	0.35	1.61	
Fe_3O_4 NPs	TMB	0.098	3.44	58
	H_2O_2	154	9.78	
HRP	TMB	0.434	10	58
	H_2O_2	3.70	8.71	

Due to its excellent peroxidase-like activity, the nanozyme was used to detect dopamine (DA) and ascorbic acid (AsA) (Fig. 7).

The introduction of DA caused the reduction of oxidized TMB (ox-TMB), as evidenced by the disappearance of the blue color and a significant decrease in its characteristic absorbance at 652 nm (Fig. S10a). The DA-induced reduction in absorbance can be attributed to two mechanisms: (1) DA directly scavenges $^{\bullet}OH$ radicals, reducing the amount available to oxidize TMB and suppressing ox-TMB formation, and (2) DA directly reduces pre-formed ox-TMB back to colorless TMB, decreasing the absorbance signal. The DA concentration was quantified by measuring the decrease in absorbance and

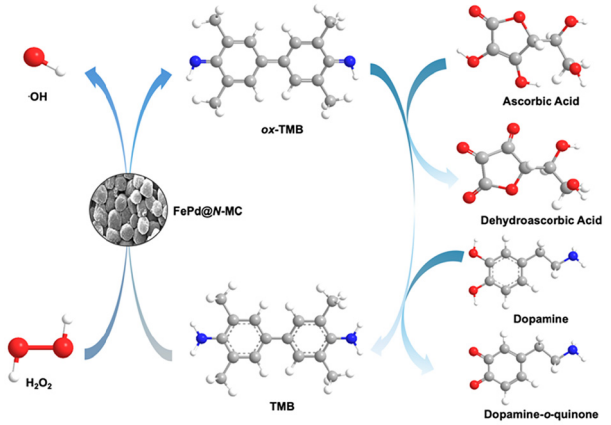

Fig. 7 Schematic illustration of the sensing platform for the analysis of AsA and DA activities.

correlating it with a standard calibration curve. A strong linear relationship was obtained between the decrease in absorbance and DA concentration in the range of 0–10 μM, with a correlation coefficient (R^2) of 0.9658 (Fig. S10b). The limit of detection (LOD), calculated using the 3σ/slope method, was determined to be 3.44 μM.

Similarly, the nanozyme was used to detect AsA. The addition of AsA also resulted in a gradual decrease in the absorbance of ox-TMB at 652 nm and fading of the blue color (Fig. 8a). This effect is mainly due to the strong reducing ability of AsA, which directly converts ox-TMB back to TMB. The absorbance change exhibited a linear relationship with AsA concentration within the 0–12 μM range, with a correlation coefficient (R^2) of 0.9831 (Fig. 8b). The LOD was calculated to be 2.87 μM.

A comparative analysis was conducted to evaluate the sensing performance of the FePd@N-MC nanozyme toward both DA and AsA. As summarized in Table 2, the achieved LODs are competitive with, and in many cases superior to, those reported in previous studies.

As shown in Fig. 8c, the presence of AsA together with other reaction components (catalyst, TMB, and H_2O_2) only delayed TMB oxidation instead of completely suppressing it. This makes precise AsA quantification more challenging. This observation can be explained by the competitive oxidation between AsA and TMB,[83,84] due to the strong electron transfer between AsA and the catalyst, in which AsA is preferentially oxidized. Control experiments confirmed this hypothesis. While AsA remained stable against oxidation by H_2O_2, its characteristic absorption at 265 nm gradually decreased in the presence of FePd@N-MC (Fig. 8d). This demonstrates an effective electron transfer interaction between AsA and the nanozyme. These results suggest that AsA does not act as a conventional radical scavenger, but rather participates directly in electron transfer with the catalyst. Accordingly, AsA was added only after complete TMB oxidation. As expected, it rapidly reduced blue ox-TMB to colorless TMB, decreasing the absorbance at 652 nm. The blue color and absorbance partially

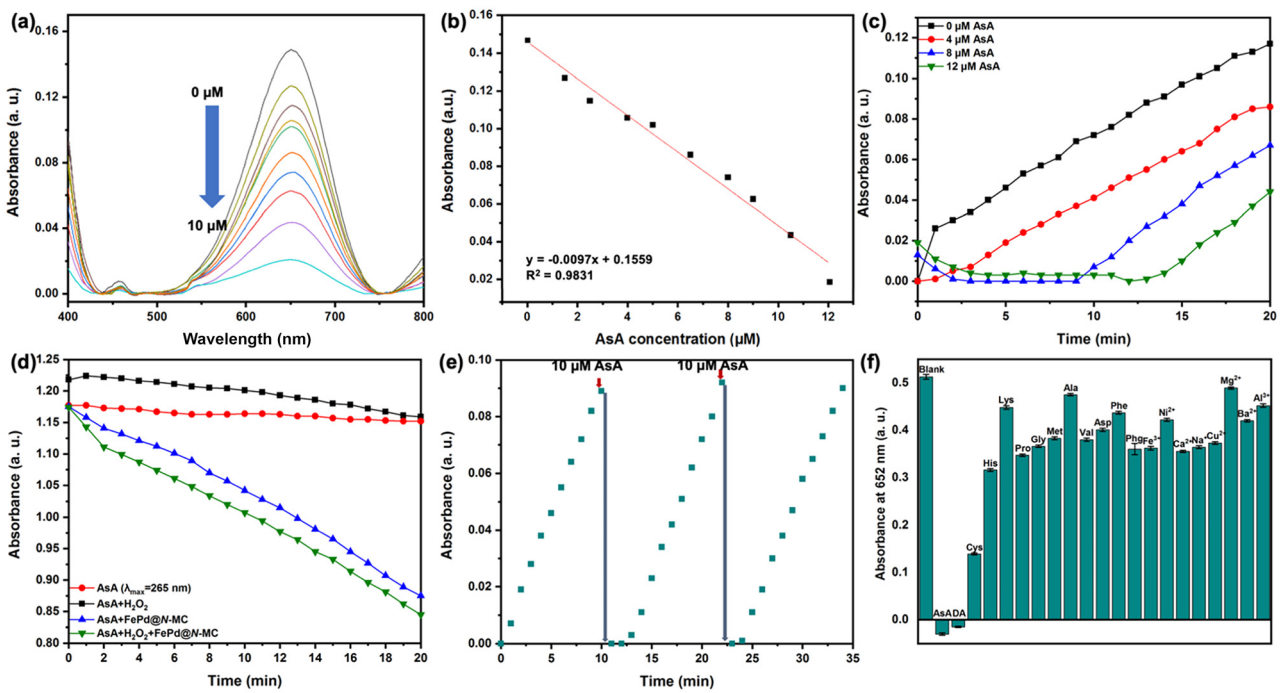

Fig. 8 (a) Absorption spectra of ox-TMB in the presence of various concentrations of AsA, (b) linear calibration curve for AsA detection, and (c) concentration-dependent inhibition effect of AsA on the peroxidase-like activity of FePd@N-MC; (d) absorbance evaluation of AsA over time in the absence and presence of H_2O_2 and FePd@N-MC; (e) continuous oxidation and reduction of TMB in the presence of the FePd@N-MC + H_2O_2 system and upon the addition of AsA. (f) Selectivity investigation of FePd@N-MC nanozymes in the presence of interfering ions and amino acids.

Table 2 Comparison of the performances of colorimetric sensors for the determination of dopamine and ascorbic acid

Catalysts	Analyte	Linear range (μM)	LOD (μM)	Ref.
GDY QDs	DA	20–100	8.65	74
SiW_9Co_3	DA	5–100	5.38	75
Cu-MOFs	DA	10–100	10	76
h-CuS NCs	DA	2–150	1.67	77
CuS-rGO	DA	2–100	480	78
Fe-CuO	AsA	5–50	4.66	79
Cu–Ag/rGO	AsA	5–30	3.6	80
$CP_{600\text{-}6}$	AsA	0.8–80	35	81
AgFKZSiW12@PPy	AsA	1–80	2.7	82
FePd@N-MCS	DA	0–10	3.44	This work
	AA	0–10	2.87	This work

recovered over time, and this cycle was repeated with successive AsA additions (Fig. 8e). This is likely due to the catalyst re-oxidizing the reduced TMB *via* its peroxidase-like activity.

The selectivity of the colorimetric assay was evaluated by measuring the absorbance at 652 nm in the presence of potential interfering substances. These substances included amino acids such as histidine (His), lysine (Lys), valine (Val), alanine (Ala), proline (Pro), glycine (Gly), aspartic acid (Asp), phenylalanine (Phe), methionine (Met), and phenylglycine (Phg), as well as various metal ions such as Na^+, Ca^{2+}, Mg^{2+}, Cu^{2+}, Fe^{3+}, Ni^{2+}, Al^{3+}, and Ba^{2+}, as shown in Fig. 8f. Among all the tested substances, both AsA and DA induced a significant response, reflected by their significantly lower absorbance signals compared to those of the interfering compounds. The notably weak responses from potential interferents validate the assay's minimal cross-reactivity and high specificity toward AsA and DA. Therefore, AsA and DA were identified as the most suitable analytes for this detection platform.

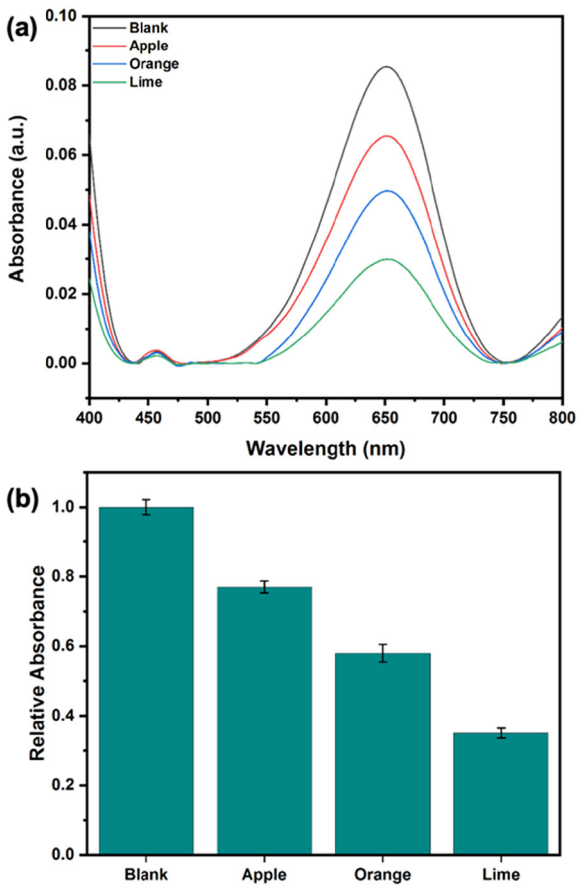

Fig. 9 (a) UV-vis absorption spectra for the detection of ascorbic acid in juice samples from various fruits; (b) a comparison of the relative absorbance change in the presence of different fruit juices.

Table 3 Determination of AsA in fresh orange juice

Added (μM)	Found (μM)	Recovery (%)	RSD% (n = 3)
0	0.17	—	1.04
1.5	1.61	96	1.86
2.5	2.80	105	2.05
4	4.07	97.5	1.93

The practical effectiveness of the AsA sensing method was assessed by analyzing fresh juice samples from apple, orange, and lime. In these experiments, FePd@N-MC, TMB, H_2O_2, and the fruit samples were mixed, and the absorbance of the solutions was measured after 15 minutes. As shown in Fig. 9, adding each fruit sample led to a noticeable decrease in the absorbance of ox-TMB. Among the tested fruits, apple juice caused the smallest decrease in absorbance, while lime juice induced a more significant decrease, indicating a higher AsA content. Orange juice exhibited an intermediate response. These results demonstrate a simple and effective strategy for the comparative analysis of AsA content in fruit samples.

The concentration of AsA in fresh orange juice was determined using the developed colorimetric system, and the recovery results are presented in Table 3. The initial AsA concentration in the unspiked sample was 6.25 μM, confirming the natural presence of ascorbic acid in fresh orange juice. For samples spiked with 1.5, 2.5, and 4 μM AsA standard, the measured concentrations were 1.61, 2.80, and 4.07 μM, respectively. The corresponding recovery rates were calculated to be 96%, 105%, and 97.5%, respectively. These results demonstrate the colorimetric system's applicability for detecting ascorbic acid in real samples. They also suggest that the developed colorimetric assay can effectively detect and quantify ascorbic acid even in complex natural matrices such as fresh orange juice.

Conclusions

In summary, this study successfully designed and synthesized the novel bimetallic FePd@N-MC nanozyme. A comprehensive analysis confirmed the formation of superparamagnetic Fe_3O_4/Pd^0 nanoparticles dispersed on the nitrogen-doped mesoporous carbon support. The FePd@N-MC nanozyme demonstrated significantly enhanced peroxidase-like activity in the

oxidation of both TMB and OPD substrates, substantially outperforming its monometallic counterparts (Fe@N-MC and Pd@N-MC). This superior activity is attributed to the strong synergistic effect between the iron and palladium species, which facilitates electron transfer and substrate interaction. Kinetic studies confirmed that the nanozyme follows Michaelis–Menten behavior. Mechanistic investigations identified the hydroxyl radical (˙OH) as the primary reactive species. Due to the nanozyme's high activity, a simple, sensitive, and selective colorimetric sensing platform was developed. The assay achieved low detection limits for both dopamine (3.44 μM) and ascorbic acid (2.87 μM). The practical utility of the nanozyme was validated by its successful application in quantifying ascorbic acid in real fruit juice samples, yielding excellent recovery rates. This work highlights the rational design of cost-effective and highly efficient bimetallic nanozymes and opens a promising approach for their use in biosensing, environmental monitoring, and medical diagnostics.

Author contributions

Zahra Bahreini: software, visualization, formal analysis, methodology, and writing – original draft. Siyavash Kazemi Movahed: supervision, project administration, funding acquisition, conceptualization, investigation, resources, and writing – review & editing. Keun Hwa Chae: writing – review & editing and formal Analysis. Cheol-Hwee Shim: formal analysis.

Conflicts of interest

There are no conflicts to declare.

Data availability

The authors confirm that the data supporting the findings of this study are available within the article or its supplementary information (SI). Supplementary information is available. See DOI: https://doi.org/10.1039/d6nr00031b.

Acknowledgements

This study was financially supported by the Research Council of Isfahan University of Technology and the Iran National Science Foundation (4022193).

References

1 E. M. Hamed, V. Rai and S. F. Y. Li, *Chemosphere*, 2024, **346**, 140557.
2 D.-M. Liu, J. Chen and Y.-P. Shi, *TrAC, Trends Anal. Chem.*, 2018, **102**, 332–342.
3 Y. Huang, J. Ren and X. Qu, *Chem. Rev.*, 2019, **119**, 4357–4412.
4 D. Jiang, D. Ni, Z. T. Rosenkrans, P. Huang, X. Yan and W. Cai, *Chem. Soc. Rev.*, 2019, **48**, 3683–3704.
5 M. Liang and X. Yan, *Acc. Chem. Res.*, 2019, **52**, 2190–2200.
6 B. Jiang, D. Duan, L. Gao, M. Zhou, K. Fan, Y. Tang, J. Xi, Y. Bi, Z. Tong, G. F. Gao, N. Xie, A. Tang, G. Nie, M. Liang and X. Yan, *Nat. Protoc.*, 2018, **13**, 1506–1520.
7 N. Yadav and S. Singh, in *Emerging Trends in Nanomedicine*, ed. S. Singh, Springer, Singapore, 2021, pp. 51–80.
8 Y. Ye, J. Zou, W. Wu, Z. Wang, S. Wen, Z. Liang, S. Liu, Y. Lin, X. Chen, T. Luo, L. Yang, Q. Jiang and L. Guo, *Nanoscale*, 2024, **16**, 3324–3346.
9 H. V. Tran, T. K. Nguyen and C. D. Huynh, *Z. Anorg. Allg. Chem.*, 2024, **650**, e202400147.
10 X. Zhu, Y. Xue, S. Hou, P. Song, T. Wu, H. Zhao, N. A. Osman, A. K. Alanazi, Y. Gao, H. M. Abo-Dief, H. Li, B. B. Xu, P. Wasnik and Q. Liu, *Adv. Compos. Hybrid Mater.*, 2023, **6**, 142.
11 X. Zhu, H. Li, S. Hou, P. Song, J. Zheng, T. Wu, H. Zhao and Q. Liu, *J. Chem. Eng.*, 2024, **482**, 148589.
12 X. Zhu, H. Li, T. Wu, H. Zhao, K. Wu, W. Xu, F. Qin, W. Chen, J. Zheng and Q. Liu, *Nano Res.*, 2022, **15**, 9319–9326.
13 R. Fu, Z. Ma, H. Zhao, H. Jin, Y. Tang, T. He, Y. Ding, J. Zhang and D. Ye, *Anal. Chem.*, 2023, **95**, 10844–10858.
14 L. Rastogi, K. Dash and R. B. Sashidhar, *Curr. Res. Biotechnol.*, 2021, **3**, 42–48.
15 R. M. Tripathi and S. J. Chung, *Luminescence*, 2023, **38**, 1330–1338.
16 I. Mustieles Marin, J. M. Asensio and B. Chaudret, *ACS Nano*, 2021, **15**, 3550–3556.
17 L. Liu and A. Corma, *Chem. Rev.*, 2023, **123**, 4855–4933.
18 S. E. Mann, L. Benhamou and T. D. Sheppard, *Synthesis*, 2015, 3079–3117.
19 X. Zhang, X. Chen, Y. Liu and M. Guo, *Water, Air, Soil Pollut.*, 2020, **231**, 277.
20 M. Hu, W. Wu and H. Jiang, *ChemSusChem*, 2019, **12**, 2911–2935.
21 C. Hui and J. Xu, *Tetrahedron Lett.*, 2016, **57**, 2692–2696.
22 L. Ouyang and W. Wu, *Curr. Opin. Green Sustainable Chem.*, 2017, **7**, 46–55.
23 R. N. d'Alnoncourt, M. Friedrich, E. Kunkes, D. Rosenthal, F. Girgsdies, B. Zhang, L. Shao, M. Schuster, M. Behrens and R. Schlögl, *J. Catal.*, 2014, **317**, 220–228.
24 A. Mansouri and N. Semagina, *Catal. Sci. Technol.*, 2018, **8**, 2323–2332.
25 Y. Cheng, H. Pham, J. Huo, R. Johnson, A. K. Datye and B. Shanks, *Mol. Catal.*, 2019, **477**, 110546.
26 J. Ge, Z. Zeng, F. Liao, W. Zheng, X. Hong and S. C. E. Tsang, *Green Chem.*, 2013, **15**, 2064–2069.
27 H. Jin, M. Cui, P. Liu, Z. Wang, T. Jin, Y. Yang, W. Zhu and X. Qian, *React. Chem. Eng.*, 2024, **9**, 2954–2962.
28 P. Kast, M. Friedrich, D. Teschner, F. Girgsdies, T. Lunkenbein, R. N. d'Alnoncourt, M. Behrens and R. Schlögl, *Appl. Catal., A*, 2015, **502**, 8–17.

29 X. Wang, J. Li, J. Xing, M. Zhang, R. Liao, C. Wang, Y. Hua and H. Ji, *J. Colloid Interface Sci.*, 2024, **656**, 104–115.
30 A. Santos, R. J. Lewis, D. J. Morgan, T. E. Davies, E. Hampton, P. Gaskin and G. J. Hutchings, *Catal. Sci. Technol.*, 2022, **12**, 2943–2953.
31 S. Fan, S. Luo, Y. Wang, X. Yue, D. Zheng, Z. Zhang, X. Fu and W. Dai, *Sep. Purif. Technol.*, 2024, **336**, 126256.
32 M. Fronczak, A. Kasprzak and M. Bystrzejewski, *J. Environ. Chem. Eng.*, 2021, **9**, 104673.
33 Y. Liu, G. Wang, W. Ma, N. Feng, J. Tong, X. Kang, T. Hu, H. Wu, Q. Yang and J. Xie, *Nanotechnology*, 2023, **34**, 465701.
34 T. R. Kumar, A. Vignesh, A. G. Al-Sehemi, M. Pannipara, S. Sutharsun, S. Suryaprakash and G. Gnana kumar, *ACS Appl. Energy Mater.*, 2023, **6**, 7445–7456.
35 Y. Zhou, L. Tang, G. Yang, G. Zeng, Y. Deng, B. Huang, Y. Cai, J. Tang, J. Wang and Y. Wu, *Catal. Sci. Technol.*, 2016, **6**, 1930–1939.
36 Z. Li, F. Liu, C. Chen, Y. Jiang, P. Ni, N. Song, Y. Hu, S. Xi, M. Liang and Y. Lu, *Nano Lett.*, 2023, **23**, 1505–1513.
37 C. Zhang, C. Chen, D. Zhao, G. Kang, F. Liu, F. Yang, Y. Lu and J. Sun, *Anal. Chem.*, 2022, **94**, 3485–3493.
38 M. Thommes, K. Kaneko, A. V. Neimark, J. P. Olivier, F. Rodriguez-Reinoso, J. Rouquerol and K. S. W. Sing, *Pure Appl. Chem.*, 2015, **87**, 1051–1069.
39 G.-H. Wang, Z. Cao, D. Gu, N. Pfänder, A.-C. Swertz, B. Spliethoff, H.-J. Bongard, C. Weidenthaler, W. Schmidt, R. Rinaldi and F. Schüth, *Angew. Chem., Int. Ed.*, 2016, **55**, 8850–8855.
40 J. Wang, H. Liu, J. Diao, X. Gu, H. Wang, J. Rong, B. Zong and D. S. Su, *J. Mater. Chem. A*, 2015, **3**, 2305–2313.
41 D. Yuan, R. B. Getman, Z. Wei, R. Q. Snurr and H.-C. Zhou, *Chem. Commun.*, 2012, **48**, 3297–3299.
42 S.-M. Wu, X.-Y. Yang and C. Janiak, *Angew. Chem.*, 2019, **131**, 12468–12482.
43 Y. Li, M. Zhao, W. Ma, T. Ma, S. Wang and X. Duan, *Chem. Eng. J.*, 2025, **504**, 156407.
44 J. Wang, L. Yang, T. Fu, F. Meng and Z. Li, *New J. Chem.*, 2022, **46**, 2980–2988.
45 W. Zhao, Y. Ye, W. Jiang, J. Li, H. Tang, J. Hu, L. Du, Z. Cui and S. Liao, *J. Mater. Chem. A*, 2020, **8**, 15822–15828.
46 L. Zhang, X. Wang, R. Wang and M. Hong, *Chem. Mater.*, 2015, **27**, 7610–7618.
47 A. P. Grosvenor, B. A. Kobe, M. C. Biesinger and N. S. McIntyre, *Surf. Interface Anal.*, 2004, **36**, 1564–1574.
48 M. N. Al-Hinai, R. Hassanien, N. G. Wright, A. B. Horsfall, A. Houlton and B. R. Horrocks, *Faraday Discuss.*, 2013, **164**, 71–91.
49 J. Rajagukguk, P. Simamora, C. S. Saragih, H. Abdullah, N. S. Gultom and A. Imaduddin, *J. Nanomater.*, 2020, **2020**, 8174871.
50 I. S. Elashmawi and H. M. Alhusaiki-Alghamdi, *Opt. Quantum Electron.*, 2024, **56**, 1090.
51 N. I. Cuello, V. R. Elías, C. E. R. Torres, M. E. Crivello, M. I. Oliva and G. A. Eimer, *Microporous Mesoporous Mater.*, 2015, **203**, 106–115.
52 J. Su, M. Cao, L. Ren and C. Hu, *J. Phys. Chem. C*, 2011, **115**, 14469–14477.
53 X. Yang, X. Zhang, Y. Ma, Y. Huang, Y. Wang and Y. Chen, *J. Mater. Chem.*, 2009, **19**, 2710–2714.
54 J. Popplewell and L. Sakhnini, *J. Magn. Magn. Mater.*, 1995, **149**, 72–78.
55 P. Srinoi, Y.-T. Chen, V. Vittur, M. D. Marquez and T. R. Lee, *Appl. Sci.*, 2018, **8**, 1106.
56 M. Gao, L. Wang, Y. Yang, Y. Sun, X. Zhao and Y. Wan, *ACS Catal.*, 2023, **13**, 4060–4090.
57 M. M. Rahman, M. G. Ara, M. A. Alim, M. S. Uddin, A. Najda, G. M. Albadrani, A. A. Sayed, S. A. Mousa and M. M. Abdel-Daim, *Int. J. Mol. Sci.*, 2021, **22**, 4498.
58 L. Gao, J. Zhuang, L. Nie, J. Zhang, Y. Zhang, N. Gu, T. Wang, J. Feng, D. Yang and S. Perrett, *Nat. Nanotechnol.*, 2007, **2**, 577–583.
59 X. Mao, F. He, D. Qiu, S. Wei, R. Luo, Y. Chen, X. Zhang, J. Lei, D. Monchaud, J.-L. Mergny, H. Ju and J. Zhou, *Anal. Chem.*, 2022, **94**, 7295–7302.
60 Y. Lu, X. Zhang and Y. Huang, *Sens. Actuators, B*, 2023, **390**, 134003.
61 X. Jia, L. Jiao, R. Li, C. Chen, X. Li, L. Hu, Y. Zhai, C. Zhu and X. Lu, *Adv. Funct. Mater.*, 2024, **34**, 2406380.
62 Y. Wu, J. Wen, W. Xu, J. Huang, L. Jiao, Y. Tang, Y. Chen, H. Yan, S. Cao, L. Zheng, W. Gu, L. Hu, L. Zhang and C. Zhu, *Small*, 2021, **17**, 2101907.
63 Y. Zhang, Y. Kang, X. Wei, C. Chen, Y. Zhai, C. Zhu, L. Jiao, X. Lu and Y. Yamauchi, *ACS Nano*, 2025, **19**, 24013–24022.
64 Y. Li, Y. Liu, X. Peng, Z. Zhao, Z. Li, B. Yang, Q. Zhang, L. Lei, L. Dai and Y. Hou, *Angew. Chem., Int. Ed.*, 2025, **64**, e202413159.
65 X. Liu, Y. Yan, Q. Zhang, H. Cai, M. Wang, X. Gong, J. Zhang, Z. Meng, H. Sun, Z. Du and X. Hao, *Adv. Funct. Mater.*, 2025, 2503345.
66 J. Huang, A. Jones, T. D. Waite, Y. Chen, X. Huang, K. M. Rosso, A. Kappler, M. Mansor, P. G. Tratnyek and H. Zhang, *Chem. Rev.*, 2021, **121**, 8161–8233.
67 Z. Shi, W. Yang, Y. Gu, T. Liao and Z. Sun, *Adv. Sci.*, 2020, **7**, 2001069.
68 A. Mahmoudi, S. K. Movahed and H. Farrokhpour, *Carbon Trends*, 2024, **17**, 100430.
69 R. Chavalala and P. Mashazi, *J. Mater. Chem. B*, 2023, **11**, 7961–7971.
70 Q. Zhang, S. Zheng, J. Zhang, W. Li and Y. Fu, *Catal. Lett.*, 2021, **151**, 2537–2546.
71 X. Li, Z. Pu, H. Zhou, W. Zhang, X. Niu, Y. He, X. Xu, F. Qiu, J. Pan and L. Ni, *J. Mater. Sci.*, 2018, **53**, 13912–13923.
72 S. Zhuo, J. Fang, C. Zhu and J. Du, *Anal. Bioanal. Chem.*, 2020, **412**, 963–972.
73 Y. Li, Y. Weng, S. Lu, M. Xue, B. Yao, W. Weng and T. Zheng, *J. Nanomater.*, 2020, **2020**, 1363212.
74 S. R. Ahmed, A. G. Cardoso, H. V. Cobas, P. Das, A. Chen, S. Srinivasan and A. R. Rajabzadeh, *ACS Appl. Nano Mater.*, 2023, **6**, 8434–8443.

75 X. Duan, Z. Bai, X. Shao, J. Xu, N. Yan, J. Shi and X. Wang, *Materials*, 2018, **11**, 674.
76 J. Wang, Y. Hu, Q. Zhou, L. Hu, W. Fu and Y. Wang, *ACS Appl. Mater. Interfaces*, 2019, **11**, 44466–44473.
77 J. Zhu, X. Peng, W. Nie, Y. Wang, J. Gao, W. Wen, J. N. Selvaraj, X. Zhang and S. Wang, *Biosens. Bioelectron.*, 2019, **141**, 111450.
78 S. Dutta, C. Ray, S. Mallick, S. Sarkar, R. Sahoo, Y. Negishi and T. Pal, *J. Phys. Chem. C*, 2015, **119**, 23790–23800.
79 B. Yan, Y. Yang, Y. Xie, J. Li and K. Li, *Chemistry*, 2023, **5**, 1302–1316.
80 G. Darabdhara, B. Sharma, M. R. Das, R. Boukherroub and S. Szunerits, *Sens. Actuators, B*, 2017, **238**, 842–851.
81 Z. Lou, S. Zhao, Q. Wang and H. Wei, *Anal. Chem.*, 2019, **91**, 15267–15274.
82 T. Wu, Z. Ma, P. Li, M. Liu, X. Liu, H. Li, Y. Zhang and S. Yao, *Talanta*, 2019, **202**, 354–361.
83 L. Han, P. Liu, H. Zhang, F. Li and A. Liu, *Chem. Commun.*, 2017, **53**, 5216–5219.
84 H. Liu, Y. He, N. Li, Z. Liu, X. Zhang, X. Zhang and Q. Liu, *ACS Appl. Bio Mater.*, 2020, **3**, 2499–2506.